ACS Photonics

pubs.acs.org/journal/apchd5

Article

Optical Control over Thermal Distributions in Topologically Trivial and Non-Trivial Plasmon Lattices

Marc R. Bourgeois, Andrew W. Rossi, Siamak Khorasani, and David J. Masiello*

Cite This: *ACS Photonics* 2022, 9, 3656−3667

Read Online

ACCESS | Metrics & More | Article Recommendations | Supporting Information

ABSTRACT: Emergent from the discrete spatial periodicity of plasmonic arrays, surface lattice resonances (SLRs) are characterized as dispersive, high-quality polaritonic modes that can be selectively excited at specific points in their photonic band structure by plane-wave light of varying frequency, polarization, and angle of incidence. Room-temperature Bose−Einstein condensation of exciton polaritons, lasing, and nonlinear matter-wave physics have all found origins in SLR systems, but to date, little attention has been paid to their thermal behavior. Here, we combine analytical theory and numerical calculations to investigate the photothermal properties of SLRs in periodic 1D and 2D arrays of plasmonic nanoparticles coupled to each other and to the electromagnetic far-field via transverse radiation. Specifically, we demonstrate how to create steady-state SLR thermal gradients spanning from the nanoscale to hundreds of microns that are actively controllable using light in spite of heat diffusion. We also demonstrate the surprising ability to localize thermal gradients at the lattice edges in topologically non-trivial SLR dimer lattices, thereby establishing a class of extraordinary thermal responses that are unconventional in ordinary materials. This work exposes a new direction in thermoplasmonics that has only just now begun to be explored.

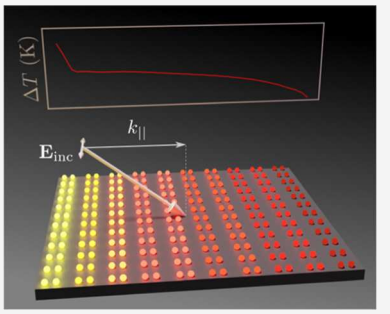

KEYWORDS: *thermoplasmonics, surface lattice resonances, photonic crystals, topological photonic materials*

1. INTRODUCTION

The ability to control heat flow and thus temperature at both nano- ($\lesssim$100 nm) and micron- ($\sim$1−10 μm) scale dimensions has important implications for a host of applications, including photothermal catalysis,[1−4] heat-assisted magnetic recording for improved data storage,[5,6] thermal encoding of encrypted data,[7−9] bolometry,[10,11] photothermal cancer therapy,[12,13] and photothermal biosensors for COVID-19,[14] among many others.[15,16] In each of these applications, photothermal control is derived from the interaction of light with noble metal nanoparticles (NPs) through excitation of their localized surface plasmon (LSP) resonances characterized by strong optical extinction. Of this extinction, the nonradiative component ultimately leads to both NP and local environment heating due to thermal diffusion.[17] Photothermal conversion via LSP decay has been studied in detail at the single NP level[18,19] as well as in assemblies of near-field-coupled NPs, demonstrating temperature increases beyond those found in individual particles.[20−22] Further ability to create and detect modified thermal profiles where heat is preferentially deposited into specific NPs within a nanoscale assembly through far-field optical excitation has also been predicted[23] and experimentally characterized[24,25] using photothermal heterodyne imaging.[26,27]

In 2013, Baffou et al.[28] showed that 2D periodic arrays of plasmonic NPs optically excited at the single particle LSP energy exhibit distinct spatial thermal profiles resulting from the interplay between heating via single particle absorption and from thermal coupling between all particles in the array. Yet it is well-known that periodic arrays of plasmonic NPs can host surface lattice resonances (SLRs) arising from hybridization of the diffractive photonic modes inherited from the array periodicity[29] with the LSPs supported by each NP in the array.[30−32] The prospects of SLR-based systems for photothermal applications is intriguing. On the one hand, optimization of such systems favors larger NP sizes to enable scattering-induced particle−particle coupling, which decreases the proportion of nonradiative decay to the overall LSP decay rate. At the same time, however, collective diffractive coupling at the center and edges of the Brillouin zone creates standing waves within the lattice leading to strongly enhanced absorption at the SLR energies.[31] Furthermore, non-Bravais lattices with >1 NP per unit cell[33−37] open the possibility for modes exhibiting hierarchical excitation and thermal spatial profiles on both the unit cell and array length scales. Careful tuning of intra- and inter-unit-cell interactions in non-Bravais NP arrays can also, under suitable conditions, lead to the existence of topologically protected hybrid modes that are

Received: July 24, 2022
Published: October 14, 2022

https://doi.org/10.1021/acsphotonics.2c01155
ACS Photonics 2022, 9, 3656−3667

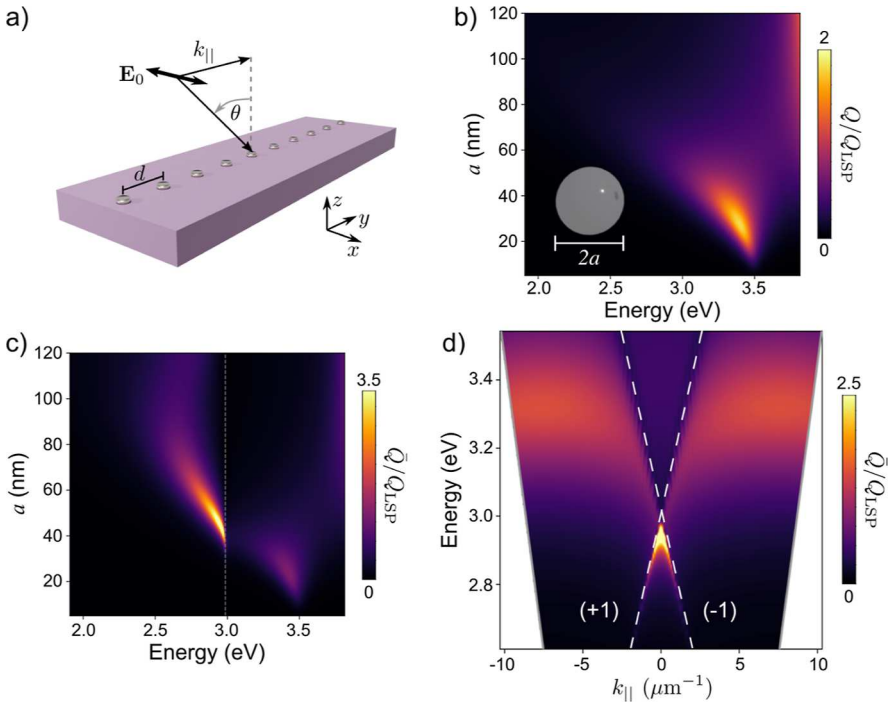

Figure 1. Electromagnetic absorption by a 1D monomer array. (a) Array scheme indicating x-polarized incident radiation propagating along the y-direction. (b) Normalized heat power absorption Q/Q_{LSP} spectra for individual Ag nanospheres in the dipole limit as a function of radius a. (c) Normalized per-particle heat power absorption $\bar{Q}/Q_{LSP}$ spectra for a 1D array of NPs with periodicity d = 415 nm as a function of radius a. The vertical dashed gray line marks the position of the Γ point Rayleigh anomaly near 3.0 eV. (d) $\bar{Q}/Q_{LSP}$ for a 1D array of a = 45 nm Ag nanospheres with periodicity d = 415 nm as a function of the Bloch vector $k_{||}$. All heat power spectra are normalized by the heat power absorbed by an a = 45 nm Ag sphere at the dipolar LSP energy Q_{LSP} at the same incident field intensity. Color bar maxima values in panels (c,d) were selected for overall plot visibility and are not the maximum values attained in the plotted domains. The maximum $\bar{Q}(k_{||} = 0, \omega)/Q_{LSP}$ value in both panels is ∼4.1.

strongly localized to the array edges,[38,39] which could potentially be exploited to achieve thermal profiles that are similarly biased toward the array edges.

Using analytical theory and numerical calculations, in this article, we investigate steady-state photothermal heating in diffractively coupled Bravais and non-Bravais plasmonic NP arrays and show how the illumination conditions can be used to actively tune thermal profiles at both nano- ($\lesssim$100 nm) and micron- (∼1−100 μm) scales. Particular attention is paid to array band structures arising from discrete translational symmetry to understand the role played by strong electromagnetic coupling during optical absorption. Nanoscale control over thermal gradients within each unit cell is also demonstrated by leveraging symmetry-dependent optical selection rules for homodimer and heterodimer non-Bravais unit cells. Finally, we raise the intriguing prospect of exploiting topologically protected edge modes to localize photothermal heating to finite array edges. Importantly, we employ a realistic treatment of material losses and long-range particle−particle coupling inherent to LSP-based systems. Taken together, this work outlines a practical set of structure-function relationships relevant to designing realistic plasmonic lattice systems for chemical, biological, medical, engineering, and technological applications.

2. PHOTOTHERMAL PROPERTIES OF 1D BRAVAIS AND NON-BRAVAIS PLASMONIC LATTICES

2.1. Bravais Arrays. The emergence of SLRs in plasmonic arrays requires NPs that are large enough to scatter appreciably, thereby providing a mechanism to lock light into the lattice plane and induce long-range dipole−dipole coupling spanning the entire lattice domain. Yet plasmonic NPs also absorb optical energy, ultimately dissipating it to heat and causing a temperature rise within the lattice and its surrounding environment. By balancing these two contributions—scattering and absorption—here we demonstrate the ability to create and manipulate long-range thermal gradients in SLR arrays that are actively controllable in steady-state through the variation of the parameters of the incident light field (i.e., frequency, direction, and polarization) despite the effects of heat diffusion.

Figure 1a illustrates a 1D plasmonic NP lattice composed of a periodic array of Ag nanospheres, each modeled as an electric dipole absorber/scatterer with dipole moment $\mathbf{p}_i$ coupled to all other nanosphere dipoles $\mathbf{p}_j$ via the relay tensor[40]

$$\vec{\mathbf{G}}(\mathbf{r}_i, \mathbf{r}_j, \omega) = \frac{e^{ikR_{ij}}}{R_{ij}}\left[\left(1 + \frac{i}{kR_{ij}} - \frac{1}{(kR_{ij})^2}\right)\vec{\mathbf{I}} + \left(-1 - \frac{3i}{kR_{ij}} + \frac{3}{(kR_{ij})^2}\right)\hat{\mathbf{R}}_{ij}\hat{\mathbf{R}}_{ij}\right] \quad (1)$$

where $\mathbf{R}_{ij} = \hat{\mathbf{R}}_{ij}R_{ij}$ is the vector connecting dipoles i and j separated by the distance $R_{ij} = |\mathbf{r}_i - \mathbf{r}_j|$ and $k = \omega\sqrt{\varepsilon}/c = 2\pi\sqrt{\varepsilon}/\lambda$ with background refractive index $\sqrt{\varepsilon}$. Though we retain this ε-dependence in all equations, we use a background medium refractive index of unity in all following calculations. In the matrix form, the coupled dipole

https://doi.org/10.1021/acsphotonics.2c01155
ACS Photonics 2022, 9, 3656−3667

equations for an N dipole system can be organized into the linear system of equations[41,42]

$$\vec{\vec{\mathbf{A}}}(\omega)\mathbf{P}(\omega) = \mathbf{E}_0(\omega) \tag{2}$$

with $3N \times 3N$ matrix $\vec{\vec{\mathbf{A}}}(\omega)$ consisting of 3×3 matrix blocks $\vec{\vec{\mathbf{A}}}_{ij}(\omega) = \alpha^{-1}(\omega)\vec{\vec{\mathbb{I}}}_{ij} - \vec{\vec{\mathbf{G}}}_{ij}(\omega)$ connecting NPs i and j. Here, $\alpha^{-1}(\omega)\vec{\vec{\mathbb{I}}}_{ij} = \vec{\vec{\boldsymbol{\alpha}}}^{-1}(\omega)\delta_{ij} = \alpha^{-1}(\omega)\vec{\vec{\mathbf{I}}}\delta_{ij}$ is a function of the isotropic dipole polarizability $\alpha(\omega) = i(3/2k^3)a_1(\omega)$ derived from the $l = 1$ Mie scattering coefficient $a_1(\omega)$. The purely off-diagonal interaction matrix $\vec{\vec{\mathbf{G}}}_{ij}(\omega) = (k^2/\varepsilon)\vec{\vec{\mathbf{G}}}(\mathbf{r}_i, \mathbf{r}_j, \omega)(1 - \delta_{ij})$ accounts for dipole−dipole coupling, and $\mathbf{P}(\omega)$ and $\mathbf{E}_0(\omega)$ are $3N \times 1$ column vectors containing the Cartesian components of the N-induced dipole moments $\mathbf{p}_i(\omega)$ and excitation field values $\mathbf{E}_0(\mathbf{r}_i, \omega)$, respectively, at positions $\mathbf{r}_1, ..., \mathbf{r}_N$.

We first consider an isolated Ag nanosphere with a dipolar absorption cross section $\sigma_{abs}(\omega) = (4\pi k/\sqrt{\varepsilon})\mathrm{Im}\alpha(\omega) - (8\pi k^4/3\varepsilon^2)|\alpha(\omega)|^2$, which dictates the heat power $Q(\omega) = \sigma_{abs}(\omega)I_0 = \sigma_{abs}(\omega)(c\sqrt{\varepsilon}/8\pi)|\mathbf{E}_0(\mathbf{r}, \omega)|^2$ absorbed under incident plane wave intensity I_0. Figure 1b shows normalized heat power absorption Q/Q_{LSP} spectra as a function of the NP radius a, where we choose Q_{LSP} to be the maximum heat power absorbed for an $a = 45$ nm NP under identical I_0. Note that this ratio of heat powers is proportional to $\sigma_{abs}(\omega)$ and does not depend on I_0. Due to the onset of dynamic depolarization and radiation damping arising from a significant scattering contribution,[43] we see that Q/Q_{LSP} increases initially for small radii, reaches a maximum at the LSP resonance energy for $a \sim 25$ nm and then begins to diminish. This behavior is well-known and underlies conventional design principles for photothermal systems, which seek to optimize the single-particle heat power.

In the case of periodic lattices, the absorption cross section and heat power inherit the energy-momentum dispersion dictated by the lattice's discrete translation symmetry. In the infinite lattice limit under plane wave illumination, the magnitudes of the induced dipole moments at each site are all equal but may adopt different directions and phase relationships determined by the coupled dipole equations in the reciprocal space[32]

$$\mathbf{p}(k_{\|}, \omega) = [\vec{\vec{\alpha}}^{-1}(\omega) - \vec{\vec{\mathbf{S}}}(k_{\|}, \omega)]^{-1}\cdot\mathbf{E}_0(k_{\|}, \omega) \tag{3}$$

which are derived from eq 2 together with the Bloch ansatz $\mathbf{p}_j = \mathbf{p}(k_{\|})e^{ik_{\|}jd}$. Here, $k_{\|}$ is the Bloch wave vector contained within the first Brillouin zone and $\vec{\vec{\mathbf{S}}}(k_{\|}, \omega) = (k^2/\varepsilon)\sum_{j\neq 0}\vec{\vec{\mathbf{G}}}(\mathbf{r}_0, \mathbf{r}_j, \omega)e^{ik_{\|}jd}$ is the field propagator tensor accounting for diffractive coupling between dipoles. Although this formalism is identical to that used in ref 44, the field propagator in the present case is a poorly convergent infinite series and special care is required to ensure convergence.[45] The total local field at the position of each dipole is then $\mathbf{E}(k_{\|}, \omega) = \vec{\vec{\alpha}}^{-1}(\omega)\cdot[\vec{\vec{\alpha}}^{-1}(\omega) - \vec{\vec{\mathbf{S}}}(k_{\|}, \omega)]^{-1}\cdot\mathbf{E}_0(\omega)$, resulting in the field enhancement

$$\left[\frac{E(k_{\|}, \omega)}{E_0}\right]_{\beta} = \frac{1}{1 - \alpha_{\beta\beta}(\omega)S_{\beta\beta}(k_{\|}, \omega)} \tag{4}$$

for an incident field polarized along the $\hat{\boldsymbol{\beta}}$-direction ($\beta = x, y, z$) in a 1D array where the orthogonally polarized lattice modes decouple. Field enhancement maxima occur for real-valued frequencies nearby the complex poles of eq 4 dictated by the condition $\alpha_{\beta\beta}^{-1}(\omega) = S_{\beta\beta}(k_{\|}, \omega)$ for $\omega \in \mathbb{C}$, which alters the spectral position of the maximum heat power absorbed relative to that of a single sphere. We capture this effect by defining an array-modified per-particle absorption cross section $\bar{\sigma}_{abs}(k_{\|}, \omega) = \sigma_{abs}(\omega)(|\mathbf{E}(k_{\|}, \omega)|^2/|\mathbf{E}_0(k_{\|}, \omega)|^2)$ such that the per-particle heat power $\bar{Q}(k_{\|}, \omega) = \bar{\sigma}_{abs}(k_{\|}, \omega)(c\sqrt{\varepsilon}/8\pi)|\mathbf{E}_0(k_{\|}, \omega)|^2$ in analogy to the single particle heat power $Q(\omega)$.

Figure 1c presents $\bar{Q}(k_{\|} = 0, \omega)/Q_{LSP}$ as a function of a and $\hbar\omega$ for a $d = 415$ nm periodicity 1D Ag NP array excited by a plane wave at normal incidence with polarization perpendicular to the periodicity direction as shown in Figure 1a. The longitudinally polarized lattice dispersion (Supporting Information) exhibits weaker coupling of the LSPs to the photonic modes because the far-field radiation lobes of each induced dipole are oriented perpendicular to the array axis, inhibiting long-range coupling.[32,46] The vertical dashed gray line in Figure 1c denotes the energy associated with the Rayleigh anomaly hc/d marking the onset of the SLR stemming from the dipolar LSP of each NP. Critically, for NP radii well-beyond that which optimize the single-particle absorption in Figure 1b, long-range diffractive coupling enabled by strong scattering contributes to enhanced absorption at the SLR mode energy. Thus, we define the single NP heat power Q_{LSP} at $a = 45$ nm. Contributions to the single-particle absorption from higher order multipoles as a function of NP radius are shown in the Supporting Information and demonstrate that the dipolar response dominates the spectrum at $a = 45$ nm. This behavior contrasts sharply from previous work on photothermal heating in NP arrays,[20,28] which considered smaller radii NPs optimized for single-particle absorption and precluded observation of robust SLR modes. Indeed, strongly enhanced photothermal conversion based on SLR modes has been recently demonstrated experimentally under normally incident excitation.[47] The dependence of $\bar{Q}(k_{\|}, \omega)/Q_{LSP}$ on the incident Bloch wave vector $k_{\|}$ for a 415 nm periodicity 1D array of $a = 45$ nm Ag nanospheres is shown in Figure 1d, demonstrating the ability to modulate photothermal heat absorption via the angle of incidence of the excitation field.

Based upon the method of coupled dipoles,[30,32,48] these calculations incorporate both scattering and absorption processes in the self-consistent determination of the lattice's optical responses. Thus, properties derived from absorption such as the temperature of the lattice can be calculated from knowledge of the heat power dissipated in each nanosphere. For a finite system of point heat sources $Q_i(\omega) = \sigma_{abs}(\omega)(c\sqrt{\varepsilon}/8\pi)|\mathbf{E}(\mathbf{r}_i, \omega)|^2$, the superposition principle can be invoked to write the total temperature at a given point $\mathbf{r}$ as a sum over discrete sources, each contributing a factor of $\Delta T(\mathbf{r}, \omega) = Q_i(\omega)/4\pi\kappa|\mathbf{r} - \mathbf{r}_i|$, where κ is the thermal conductivity of the surrounding medium and $\mathbf{E}(\mathbf{r}_i, \omega)$ is the total local field (incident plus that contributed by the other $N - 1$ dipoles) at the position of the ith dipole. All thermal calculations in this work employ the incident plane wave intensity $I_0 = 10^8$ W/m^2 and a thermal conductivity $\kappa = 0.6$ W m^{-1} K^{-1} similar to water. Similar to previous work,[23−25] the

https://doi.org/10.1021/acsphotonics.2c01155
ACS Photonics 2022, 9, 3656−3667

effect of thermal radiation is neglected in our calculations, as its contribution is negligible relative to thermal conduction. For non-vanishing source radii within the uniform temperature approximation,[28,49] the internal temperature increase of nanosphere i due to nanosphere j is found by spatially averaging the thermal field due to the nanosphere at $\mathbf{r}_j$ over the volume of the nanosphere at $\mathbf{r}_i$. Under the uniform temperature approximation, the total internal temperature increase of nanosphere i is then

$$\Delta T(\mathbf{r}_i, \omega) = \frac{Q_i(\omega)}{4\pi\kappa a} + \sum_{j\neq i} \frac{Q_j(\omega)}{4\pi\kappa|\mathbf{r}_i - \mathbf{r}_j|} \tag{5}$$

where the first and second terms account for direct optical absorption ΔT_{opt} and thermal coupling ΔT_{th} contributions to the total internal temperature, respectively. Naturally, the ratio of these two terms at a common frequency

$$\zeta_i = \frac{\Delta T_{opt}}{\Delta T_{th}} = \left(\frac{a}{Q_i}\sum_{j\neq i}\frac{Q_j}{|\mathbf{r}_i - \mathbf{r}_j|}\right)^{-1} \tag{6}$$

defines a unitless quantity of interest with $\zeta \gg 1$ and $\zeta \ll 1$ characterizing qualitatively different temperature profiles.[28] Specifically, the temperature increase is highly localized in the vicinity of the particles for $\zeta \gg 1$, while there is significant ΔT in regions between particles for $\zeta \ll 1$. Baffou showed[28] that the value of this ratio of thermal contributions in the central unit cell of a finite array of N monomer unit cells can be analytically approximated as

$$\zeta_{1D} = \left[\frac{2a}{d}\sum_{i=1}^{(N-1)/2}\frac{1}{i}\right]^{-1} \approx \frac{d}{2a\log N} \tag{7}$$

when $Q_i = Q$ for all $i = 1, ..., N$ in eq 6. While this is expected to be a good approximation for systems of small particles with negligible scattering-induced particle−particle coupling, one may anticipate $Q_i \neq Q_j$ for all i, j in finite arrays with strong particle−particle coupling. On the other hand, the Bloch ansatz ensures $Q_i = Q_j = \bar{Q}$ for all i, j in the infinite lattice limit, but this necessitates $N \to \infty$ and causes $\zeta_{1D} \to 0$ in eq 7, signaling a breakdown of the model arising from the infinite total heat delivered to the unbounded system. Together, these observations motivate the examination of ζ_i in realistic finite lattice systems supporting SLRs.

To explore how the ratio of ΔT_{opt} to ΔT_{th} evolves for finite arrays, we consider an 83 μm array composed of 201 unit cells with a = 45 nm Ag NPs and d = 415 nm periodicity. Figure 2a shows the ζ_0 evolution as the number of NPs illuminated in the array center at the SLR energy (~2.95 eV) is varied at normal incidence. The ratio ζ_0 is calculated using the site space coupled dipole method (eq 2) to evaluate eq 6 explicitly for the central unit cell i = 0 (colored bullets) and compared against the approximate expression eq 7 (dashed gray) with N determined by the illumination width and the array periodicity d. Figure 2a demonstrates that $\zeta_0 \sim 1$ for the SLR system considered and that the contribution of ΔT_{th} to the total ΔT does increase for the particle in the center of a partially illuminated finite array as the illumination width increases. It is also evident that the approximate expression in eq 7 accurately predicts ζ_0 for the finite, partially illuminated system. Nevertheless, eq 7 is of limited practical utility as it only reports on the temperature increase contributions for the unit cell at the center of the array.

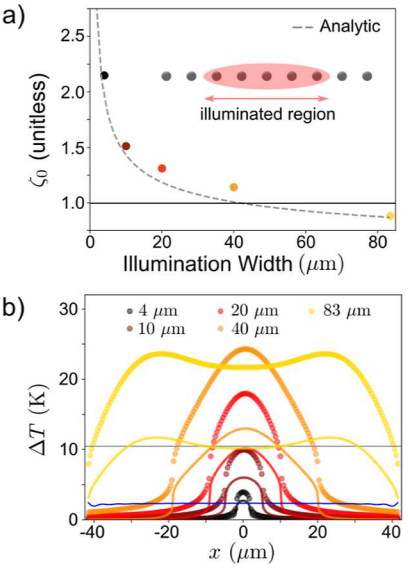

Figure 2. Direct optical and thermal coupling contributions to photothermal heating in finite 1D arrays. (a) Evolution of ζ_0 as the width of the illuminated region at the center of an 83 μm finite array is varied. The array parameters are identical to those of Figure 1d. The dashed gray line is the analytic approximation in eq 7. (b) Total ΔT (bullets) and ΔT_{opt} contribution (lines) for $k_{\|}$ = 0 excitation at the SLR energy near 2.95 eV as a function of illumination width. The horizontal gray line indicates the value of ΔT_{opt} in the infinite lattice limit, while the blue line shows ΔT for full illumination of the finite array at the single LSP energy near 3.3 eV. The incident laser intensity is $I_0 = 10^8$ W/m^2.

Figure 2b presents the total ΔT (bullets) and associated ΔT_{opt} (lines) contribution at each particle site for $k_{\|}$ = 0 excitation at the SLR energy as a function of illumination width (color coded). The trace and bullet colors in panel (b) indicate the illumination width and match the bullet colors used in panel (a). The horizontal dashed gray line marks the value of ΔT_{opt} in the infinite lattice limit obtained using the reciprocal space coupled dipole equations to evaluate $\bar{Q}(k_{\|} = 0, \omega)$ at the SLR frequency. The nearly horizontal blue line indicates ΔT at each NP when excited at the single-NP LSP energy. As one might expect, the gray line is ~4× larger than the blue line because $\bar{Q}/Q_{LSP} \sim 4$ in Figure 1c,d. Inspection of Figure 2b shows that direct optical absorption heating dominates for small illumination regions. When the illumination width reaches 20 μm in this system, ΔT_{opt} has reached the infinite lattice limit at the central unit cell, but rapidly falls off away from the array center. As the illuminated width continues to increase, ΔT_{opt} remains approximately equal to the infinite lattice limit at the center of the array, but the number of unit cells away from array center attaining this value also increases. Ultimately, it is this saturation of ΔT_{opt} along with the increase of the number of heated sites that increases ΔT_{th} and decreases ζ_0 in Figure 2a as the illumination width grows.

2.2. Non-Bravais Dimer Arrays. Further control over the photothermal conversion process can be achieved through the introduction of additional degrees of freedom associated with the unit cell design. The non-Bravais dimer lattice, for example, involves two sublattices (labeled A and B) with both intra- and inter-sublattice couplings between the plasmonic dipoles on

https://doi.org/10.1021/acsphotonics.2c01155
ACS Photonics 2022, 9, 3656−3667

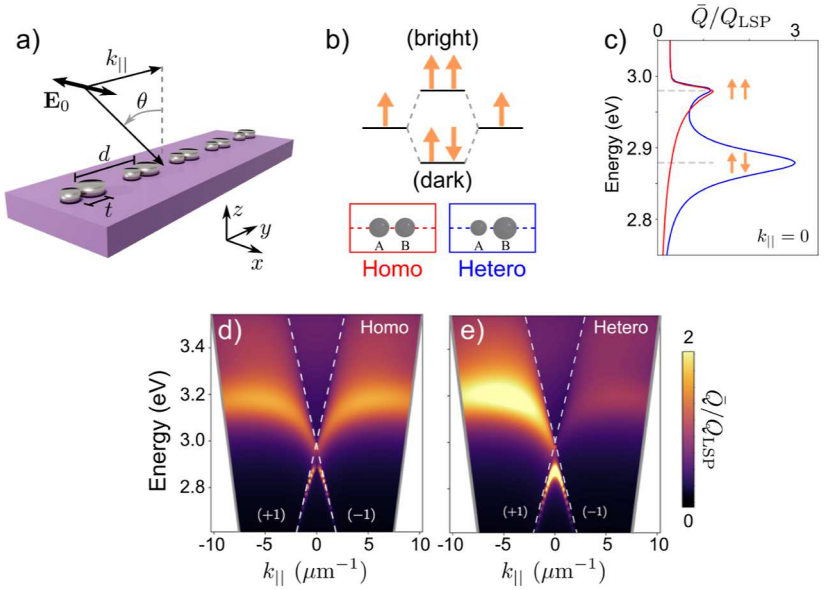

Figure 3. Non-Bravais dimer arrays with homo- and heterodimer unit cells. (a) Scheme of 1D dimer array with unit cell and dimer spacings d and t, respectively, excited by a transversely polarized plane wave. (b) Energy ordering of hybridized transverse dipoles on sites A and B within each unit cell. (c) Normalized per-NP heat power absorption $\bar{Q}/Q_{LSP}$ spectra for the 1D array at the Γ point for homo- (red) and heterodimer (blue) unit cells. (d,e) $\bar{Q}/Q_{LSP}$ as function of $k_{||}$ for arrays with homo- and heterodimer unit cells, respectively. In panels (c−e), d = 415 nm and t = 120 nm. The particle radii are $a_A = a_B$ = 45 nm for the homodimer structure, while a_A = 40 nm and a_B = 50 nm for the heterodimer structure.

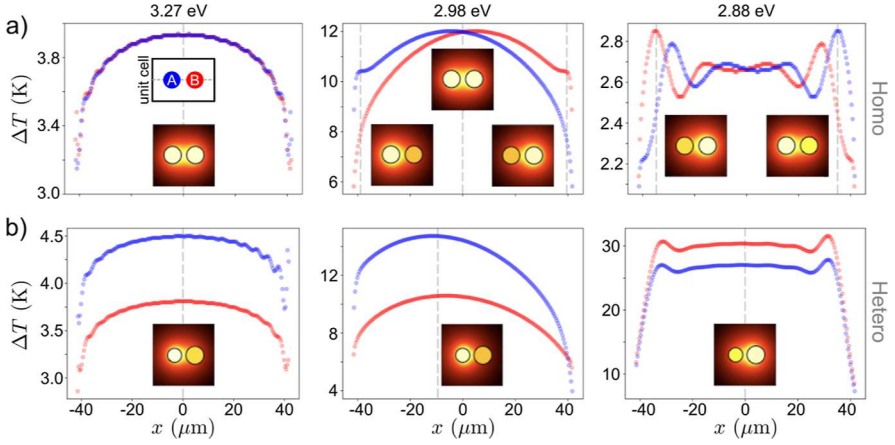

Figure 4. Spatial photothermal profiles for 1D non-Bravais dimer arrays. (a,b) Show ΔT at each lattice site in the finite 83 μm array with homo- and heterodimer unit cells, respectively, of Figure 3c−e illuminated at $k_{||} = 0$. Blue (red) markers indicate the internal temperature increase at the A (B) sites within each unit cell. Examples of the spatial profile of ΔT within specific unit cells at positions marked by vertical dashed gray lines are included, where $a_A = a_B$ = 45 nm and a_A = 40 nm and a_B = 45 nm for the homo- and heterodimer unit cells, respectively. The incident laser intensity is $I_0 = 10^8$ W/m^2.

each NP, which are governed by distances t and d, respectively; see Figure 3a. In the site space, the coupled dipole equations remain of the same form as those presented in eq 2 except for the case of the heterodimer unit cell where dipoles on each sublattice have different Mie polarizabilities depending upon the radius and dielectric composition of each nanosphere. It is because of their differing polarizabilities that the heterodimer lattice hybridization (Figure 3b) produces two optically bright SLRs, while only the in-phase LSP mode forms a bright SLR in the case of the homodimer lattice. This difference is highlighted in Figure 3c, which shows $\bar{Q}(k_{||} = 0, \omega)/Q_{LSP}$ spectra at the Γ point for the homodimer (red) and heterodimer (blue) lattices of Ag nanospheres with d = 415 nm and t = 120 nm. The radii of the spherical NPs are $a_A = a_B$ = 45 nm for the homodimer, while a_A = 40 nm and a_B = 45 nm for the heterodimer. Figure 3d,e displays the band dispersion of the homodimer and heterodimer lattices excited by transversely polarized plane waves. The asymmetry in incident angle (or equivalently $k_{||}$) in the dispersion of the heterodimer lattice is again due to the intrinsic asymmetry of the unit cell itself, which will be exploited below to control the temperature profile on the $\lesssim$ 100 nm scale.

Based on these SLR absorption spectra, Figure 4a shows the computed thermal profiles induced by normal incidence plane wave excitation at varying energies corresponding to spectral features in Figure 3d for the homodimer lattice at $k_{||} = 0$. When excited near the isolated dimer LSP resonance (3.27 eV), sites A and B have the same temperature ($\Delta T_A = \Delta T_B$); however, in moving across the lattice, the temperature profile changes, with dimers in the middle of the array hotter than those at the

https://doi.org/10.1021/acsphotonics.2c01155
ACS Photonics 2022, 9, 3656−3667

edges. Alternatively, at the lattice's diffractive Γ point resonances (2.98 and 2.88 eV), our calculations indicate significant and controllable temperature differences not only within each unit cell ($\Delta T_A \neq \Delta T_B$) but also across the entire lattice (e.g., there are regions where $\Delta T_A > \Delta T_B$ and others with $\Delta T_A < \Delta T_B$). Similar trends are noted in the heterodimer case (Figure 4b), although here we find that the temperature of one particle within the unit cell (either at site A or site B) consistently exceeds the other for nearly all positions across the lattice. Taken together, these results demonstrate the ability to harness dispersive SLR modes to create non-uniform thermal gradients spanning both intra-unit cell ($\lesssim$ 100 nm) and lattice (∼100 μm) distances that are actively controllable via changes in the incident angle, energy, and polarization state of light.

3. PHOTOTHERMAL PROPERTIES OF EDGE-LOCALIZED MODES IN 1D AND 2D NON-BRAVAIS HOMODIMER LATTICES

Beyond the SLR-enabled thermal profiles demonstrated in the preceding section, here we introduce an entirely new class of edge-localized temperature gradients created by tuning the homodimer lattice toward a topologically non-trivial regime. Considerable research effort has recently been expended to understand the topological properties that can emerge from arrays of plasmonic NPs[39,50−58] operating in the visible and infrared regions of the electromagnetic spectrum. However, unlike the topological Hermitian model system of Su, Schrieffer, and Heeger (SSH) describing 1D periodic arrays with two sites (A and B) per unit cell and nearest-neighbor coupling,[59] Hamiltonians describing plasmonic arrays are fundamentally non-Hermitian due to the radiative and nonradiative damping of each NP.[60−62] Additionally, frequency-dependent NP−NP interactions include vector-valued near, intermediate, and far-field components that go beyond the nearest neighbor scalar coupling assumed in the SSH Hamiltonian.[32,63] Despite these added complexities, certain plasmonic lattices have been shown to possess topologically protected edge modes exhibiting a bulk-edge correspondence,[50,62,64] meaning that properties of the infinite bulk predict the existence (or lack thereof) of edge-localized states in any finite segment of the bulk.

Fundamental to the existence of topologically protected edge states are bulk topological invariants such as the complex-valued Zak phase for one-dimensional systems[65]

$$\gamma_\beta = i\int_{-\pi/d}^{\pi/d} [\hat{\boldsymbol{\beta}}\cdot\mathbf{p}_A^L(k_\parallel)\,\hat{\boldsymbol{\beta}}\cdot\mathbf{p}_B^L(k_\parallel)]^* \frac{d}{dk_\parallel}\begin{bmatrix}\mathbf{p}_A^R(k_\parallel)\cdot\hat{\boldsymbol{\beta}}\\ \mathbf{p}_B^R(k_\parallel)\cdot\hat{\boldsymbol{\beta}}\end{bmatrix} dk_\parallel \tag{8}$$

here extended to accommodate uncoupled vector modes polarized along $\beta = x, y, z$ and constructed from components of the left $\mathbf{P}^L(k_\parallel, \omega)$ and right $\mathbf{P}^R(k_\parallel, \omega)$ reciprocal space eigenvectors. We consider a non-Bravais homodimer lattice involving two sublattices (A and B) with both intra- and inter-sublattice couplings between the plasmonic dipoles on each NP. Using the Bloch ansatz $\mathbf{p}_j^A = \mathbf{p}_A(k_\parallel)e^{ik_\parallel jd}$ and $\mathbf{p}_j^B = \mathbf{p}_B(k_\parallel)e^{ik_\parallel jd}$, the reciprocal space eigen problem is

$$\begin{aligned} 0 &= \ddot{\mathcal{A}}(k_\parallel, \omega)\cdot\mathbf{P}(k_\parallel, \omega)\\ &= \begin{bmatrix}\ddot{\alpha}^{-1}(\omega) - \ddot{\mathbf{S}}(k_\parallel, \omega) & -\ddot{\mathbf{T}}_{AB}(k_\parallel, \omega)\\ -\ddot{\mathbf{T}}_{BA}(k_\parallel, \omega) & \ddot{\alpha}^{-1}(\omega) - \ddot{\mathbf{S}}(k_\parallel, \omega)\end{bmatrix}\begin{bmatrix}\mathbf{p}_A(k_\parallel)\\ \mathbf{p}_B(k_\parallel)\end{bmatrix}\\ &= \left(\begin{bmatrix}\ddot{\alpha}^{-1}(\omega) & 0\\ 0 & \ddot{\alpha}^{-1}(\omega)\end{bmatrix} - \ddot{\mathcal{G}}(k_\parallel, \omega)\right)\begin{bmatrix}\mathbf{p}_A(k_\parallel)\\ \mathbf{p}_B(k_\parallel)\end{bmatrix}\end{aligned} \tag{9}$$

where $\ddot{\mathbf{S}}(k_\parallel, \omega) = (k^2/\varepsilon)\sum_{j\neq 0}\ddot{\mathbf{G}}(jd, \omega)e^{ik_\parallel jd}$ and $\ddot{\mathbf{T}}_{AB/BA}(k_\parallel, \omega) = (k^2/\varepsilon)\sum_j \ddot{\mathbf{G}}(jd \pm t, \omega)e^{ik_\parallel jd}$ with $j \in \mathbb{Z}$ indexing the unit cells. Due to the large NP radii and transverse coupling, the $\ddot{\alpha}^{-1}(\omega)$, $\ddot{\mathbf{S}}(k_\parallel, \omega)$, and $\ddot{\mathbf{T}}_{AB/BA}(k_\parallel, \omega)$ matrix elements are nonlinear, transcendental functions of the frequency ω and cannot be accurately linearized by evaluation at the quasistatic LSP resonance frequency ($\omega = \omega_{sp}$).[66] Details of how we solve this 6 × 6 nonlinear eigenproblem to obtain eigenenergies and eigenvectors are discussed in the Methods section.

Reference 67 shows that for a non-Hermition SSH model with nearest-neighbor coupling, the complex Zak phase can be expressed in the more compact form $\gamma_\beta = [\phi^\beta_{k_\parallel=X} - \phi^\beta_{k_\parallel=-X}]/2$, where $\phi^\beta_{k_\parallel}$ is the relative phase between induced dipole moment components on sublattice sites A and B for the right (or left) reciprocal space eigenvectors at Bloch vector $k_\parallel$. Although this simple method of evaluating γ_β is strictly valid only in the case of nearest-neighbor coupling, it has been used successfully to predict the existence of topologically protected edge-localized modes in longitudinally coupled 1D plasmonic arrays involving small particles.[50] It must be pointed out, however, that although long-range dipolar coupling does not affect the quantization of the Zak phase, it does break the underlying chiral symmetry possessed by the corresponding nearest-neighbor coupling model, which underlies the existence of the bulk-boundary correspondence.[50,64] Certain finite plasmonic arrays have been identified, for example, that do not possess gapless, edge-localized eigenvectors despite the corresponding bulk system having a Zak phase of π.[64] Nevertheless, leveraging topologically protected edge states to localize photothermal heating to array edges remains an intriguing prospect.

We now investigate the photothermal properties of a new 1D homodimer lattice with d = 250 nm, t = 100 nm, and a = 45 nm Ag spheres at each site. These parameters are chosen to tune the bulk lattice into a non-trivial topological regime characterized by a complex Zak phase $\gamma_\perp = \pi$ ($\perp = x, z$ because both transverse modes are equivalent by symmetry) as computed using our nonlinear reciprocal space eigensolver. Figure 5a displays the normalized per-particle heat power absorbed $\overline{Q}/Q_{LSP}$ as a function of $k_\parallel$ (underlying color map) of a lattice with 100 unit cells (N = 200 particles) having the same periodicity as the bulk under plane wave illumination. The optical polarization is again transverse to the lattice direction, thereby stimulating only the transversely coupled SLR modes associated with strong long-range interactions. The overlaid empty white circles indicate the real parts of the transverse eigenenergies determined using the reciprocal space eigensolver, while the red bullets on the $k_\parallel < 0$ region of Figure 5a show the real parts of the transverse eigenenergies calculated from diagonalization of the 10-unit cell finite lattice

https://doi.org/10.1021/acsphotonics.2c01155
ACS Photonics 2022, 9, 3656−3667

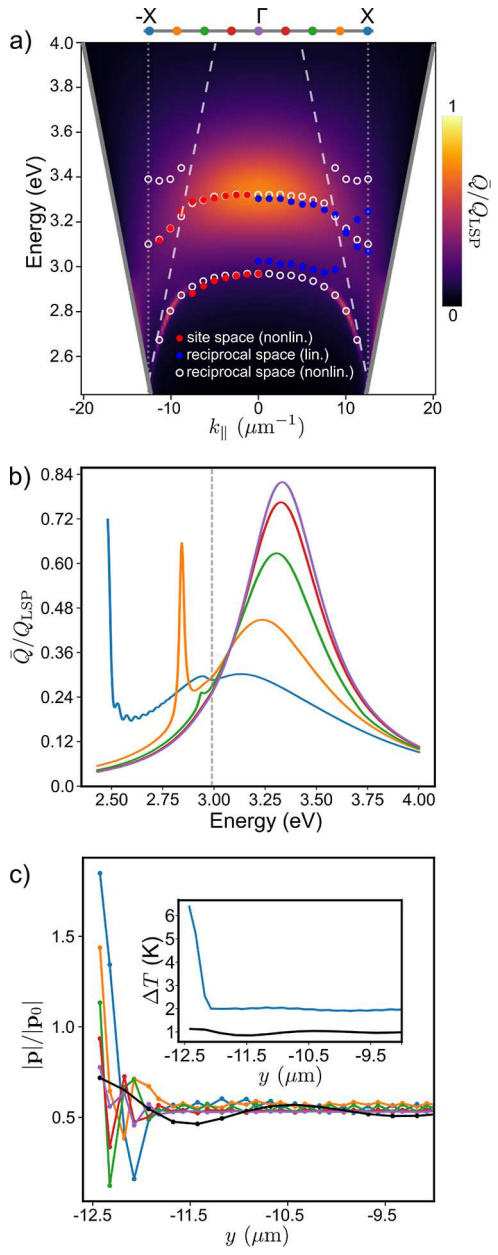

Figure 5. 1D homodimer array response. (a) Normalized per-particle heat power absorption $\bar{Q}/Q_{LSP}$ spectra as a function of $k_{\|}$ for a 1D homodimer array composed of a = 45 nm Ag nanospheres. The sublattice periodicity d = 250 nm and the dimer gap t = 100 nm. The red bullets represent the eigenenergies in the site space, while the white and blue bullets depict the nonlinear and linearized eigenenergies of the infinite lattice, respectively. (b) $\bar{Q}/Q_{LSP}$ spectra for points in reciprocal space indicated by the legend above panel (a). (c) Modulus of the induced plasmonic dipole moment on each nanosphere normalized to the induced dipole moment of a single a = 45 nm Ag nanosphere. The inset shows the spatial photothermal profile of the homodimer (blue trace) and monomer (black trace) lattices at the X point. The incident laser intensity is $I_0 = 10^8$ W/m^2.

system, both in the absence of external forcing (Methods). To sort finite lattice eigenenergies in $k_{\|}$ (red bullets), their spatial mode frequencies are examined, allowing us to overlay them on top of the $k_{\|}$-resolved absorption spectra (Supporting Information). Approximate reciprocal-space eigenenergies obtained by linearizing the coupling tensors ($\vec{\mathbf{S}}$ and $\vec{\mathbf{T}}$) at $\omega = \omega_{sp}$ in eq 9 are shown as blue bullets on the $k_{\|} > 0$ region of Figure 5a for comparison.

Figure 5b displays $\bar{Q}/Q_{LSP}$ spectra for selected points in reciprocal space, where the dip at 2.99 eV (dashed gray line) at the X point denotes the presence of an SLR band gap where an edge-localized mode might be expected[50] in finite segments of the infinite system. However, despite the infinite system having $\gamma_{\perp} = \pi$, none of the finite system eigenvectors associated with the red bullets in Figure 5a are found to be localized to the array edges (Supporting Information), indicating this system is in the regime where the bulk-boundary correspondence breaks down.[64] This is, perhaps, not surprising, because strong intra-sublattice (i.e., A−A and B−B) coupling drives the breakdown of the bulk-boundary correspondence,[39,64,68−72] while SLRs generally involve transverse modes associated with strong intra-sublattice coupling characterized by $\vec{\mathbf{S}}(k_{\|}, \omega)$.[32] Nevertheless, Figure 5c illustrates the existence of edge-localized induced dipole moments in the optically excited system. The induced dipole moments $\mathbf{p}$ are normalized to the induced dipole moment $\mathbf{p}_0$ of a single a = 45 nm Ag nanosphere excited at the same energy. Recall that in the electric dipole approximation $\mathbf{p}_i = \vec{\alpha}(\omega)\cdot\mathbf{E}(\mathbf{r}_i)$ and $\Delta T_{opt} \propto |\mathbf{E}(\mathbf{r}_i)|^2$, the induced dipole moment spatial distribution reports on the direct optical heat power delivered to each lattice site. The black line represents the dipolar profile of a 100 unit cell (200 particle) monomer lattice, that is, a 1D array of nanospheres equally spaced with periodicity $d = t$ = 250 nm. We find that while all of the selected points in reciprocal space (colored bullets above Figure 3a) exhibit dipole moment distributions with some degree of edge localization, the X point profile (blue) clearly shows the strongest edge-localization. The persistence of edge-localization at other points in the reciprocal space and at other energies is likely indicative of the non-Hermitian skin effect.[68]

Leveraging such induced dipole moment spatial profiles has the potential to produce edge-localized thermal gradients independent of whether the observed edge-localized induced dipole moments are indicative of strict topological protection or not. While previous work has examined radiative heat transfer in plasmonic lattices tuned into the topological regime,[73] we are not aware of any studies exploring the possibility of exploiting these systems to realize edge-localized temperature profiles. The inset of Figure 5c shows such a thermal profile, obtained by plane-wave excitation of the homodimer lattice at the X point at 2.99 eV (blue) in comparison to the monomer lattice (black) at the same point in the Brillouin zone. The edges of the homodimer lattice have a 3-fold temperature increase relative to the approximately constant temperature within the lattice interior.

We next investigate the photothermal properties of a finite 2D homodimer lattice assembled by arranging side-by-side copies of the topologically non-trivial 1D homodimer arrays considered in Figure 5. Figure 6b shows the normalized per-particle heat power absorption $\bar{Q}/Q_{LSP}$ spectra as a function of k_y for x-polarized plane wave illumination. The finite lattice is composed of 20 dimer unit cells oriented along the y-direction which are replicated 20 times along the x-direction. Thus, the x-polarized excitation couples to the transversely polarized SLRs with respect to the dimer unit cell axis along $\hat{\mathbf{y}}$ and the edge localization of ΔT intrinsic to each 1D component is inherited by the 2D lattice. Figure 6c,d shows the 2D

https://doi.org/10.1021/acsphotonics.2c01155
ACS Photonics 2022, 9, 3656−3667

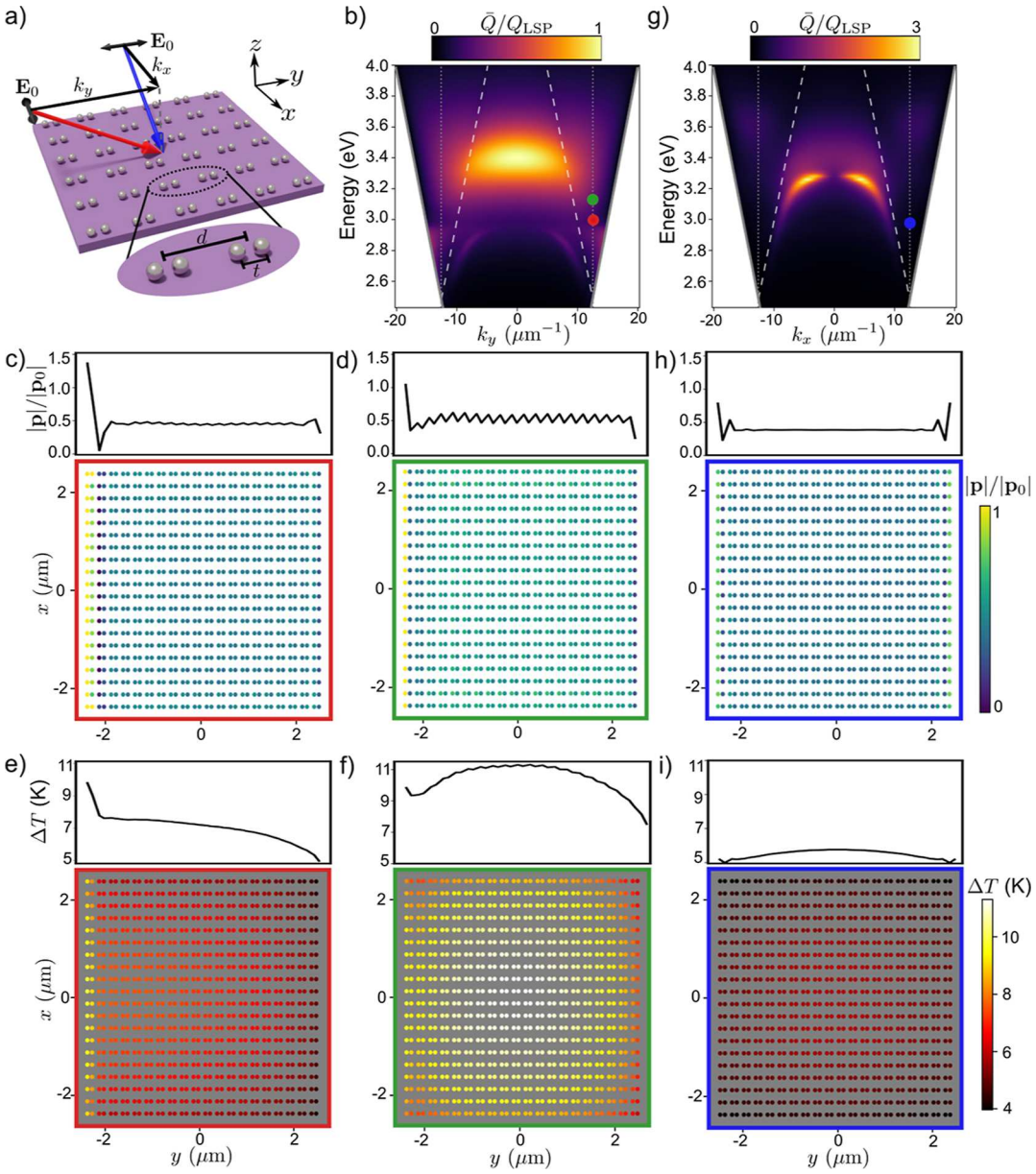

Figure 6. 2D homodimer unit cell array response. (a) Array scheme indicating the two excitation geometries considered. The 2D array is composed from replicas of the 1D array from Figure 5 with $d_x = d_y = 250$ nm and $t_y = 100$ nm. (b) Normalized per-particle heat power absorption $\bar{Q}/Q_{LSP}$ spectra as a function of k_y for a finite 20 × 20 unit cell patch of the 2D array. (c,d) Magnitude of the induced dipole moment on each nanosphere normalized to the induced dipole moment of a single $a = 45$ nm Ag nanosphere at the points marked by red and green dots, respectively, in panel (b). (e,f) Internal temperature increase corresponding to the preceding induced dipole moment plots. (g) $\bar{Q}/Q_{LSP}$ as a function of k_x for the 2D dimer array. (h) Normalized magnitude of the induced dipole moment on each nanosphere at the point marked in blue in panel (g). (i) Spatial map of the thermal profile corresponding to the induced dipole moment distribution in the preceding panel. The incident laser intensity is $I_0 = 10^8$ W/m^2.

polarizations induced at the X point at two different energies, 2.99 eV (red) and 3.13 eV (green). Each point is indicated by a bullet in Figure 6b. Panel (c) possesses stronger edge-localization of $|\mathbf{p}|/|\mathbf{p}_0|$ with $\Delta T_{opt} \propto |\mathbf{p}|^2$ in comparison to panel (d). Panels (e) and (f), which include thermal coupling contributions ΔT_{th}, account for conductive heat flow from the surrounding NPs, leading to the largest ΔT_{th} contribution at the array center. Nevertheless, some degree of edge localization on the left lattice edge persists. By rotating the excitation field so that its in-plane wave vector projects entirely along the x-direction, Figure 6g shows $\bar{Q}/Q_{LSP}$ as a function of k_x generated under y-polarized plane-wave illumination of the same 2D homodimer lattice. Under this excitation geometry, the longitudinally coupled dimer mode is excited within each unit cell, setting up diffractive SLR coupling along the x-direction. By exciting the lattice at the $k_x = \pi/dX$ point at 2.99 eV, Figure 6h shows a weakly edge-localized induced polarization, with a modest and spatially delocalized thermal profile (Figure 6i). Together, Figures 5 and 6 highlight the potential of exploiting topologically protected edge modes to spatially localize thermal profiles to finite 1D and 2D array edges, thus establishing a new class of thermal responses that differ significantly from our conventional experiences of heat flow and associated temperature rise.

https://doi.org/10.1021/acsphotonics.2c01155
ACS Photonics 2022, 9, 3656−3667

4. CONCLUSIONS

Endowed with strong energy-momentum dispersion, broad spatial delocalization, and high-quality factors, SLRs offer unexplored potential for transducing optical energy into tailored thermal gradient profiles that are robust in the steady state, even in the presence of heat diffusion. Harnessing this potential, we combine analytical theory and numerical calculations to investigate the photothermal properties of SLRs in a variety of diffractively coupled Bravais and non-Bravais plasmonic NP lattices and demonstrate the ability to exert control over their induced temperature field spanning from nano- to micron-scale dimensions by varying the energy, angle, and polarization of incident radiation. By examining the photonic band structure and associated eigenmodes of an infinite non-Bravais homodimer lattice tuned into its topologically non-trivial regime, we additionally present numerical evidence for the creation of thermal gradient profiles that are localized to the edges of a finite patch of the lattice, thus establishing a new class of thermal responses that differ significantly from our conventional experiences of heat flow and associated temperature rise.

Beyond changing the wavelength of incident light or the lattice periodicity to influence SLR response, other approaches can be implemented to control the thermal spatial distribution within each unit cell as well as across the entire lattice domain. For example, stretching/compressing the array or coupling light to higher-order multipoles in each NP[74−76] represent two additional strategies of practical utility. Employing more complex non-Bravais unit cells such as plasmon oligomers[46,77−79] represents another, indicating the high degree of tunability offered by plasmon lattices for studying photothermal conversion. Leveraging these properties, we anticipate SLR arrays to provide a new platform for studying a variety of photothermal applications in the catalytic, energy, chemical, and biological sciences and engineering.

5. METHODS

5.1. Numerical Solution of the Nonlinear Eigenvalue Problem. In the dipole limit, inspection of the coupled dipole equations shows that the complex-valued eigenfrequencies of the fully coupled (i.e., each dipole i interacts with every other dipole j) finite 1D homodimer array are dictated by the condition $\det\vec{\mathbf{A}}(\omega_n) = 0$, where the ijth block of the $3N \times 3N$ site-space matrix $\vec{\mathbf{A}}(\omega)$ is given by

$$\vec{\mathbf{A}}_{ij}(\omega) = \alpha^{-1}(\omega)\vec{\mathbb{I}}_{ij} - \vec{\mathbb{G}}_{ij}(\omega) \tag{10}$$

for an N dipole system. The diagonal inverse polarizability matrix $\alpha^{-1}(\omega)\vec{\mathbb{I}}$ and purely off-diagonal particle−particle coupling matrix $\vec{\mathbb{G}}(\omega)$ are defined below eq 2 above. Written in this form, it is clear that the system possesses an eigenvalue $\alpha^{-1}(\omega_r)$ when a complex-valued frequency ω_r can be found such that $\det\vec{\mathbf{A}}(\omega_r) = 0$. In general, this constitutes a generalized nonlinear eigenproblem and it is difficult to locate such eigenfrequencies. Pocock et al.[50] addressed this challenge by employing a linearization approximation that eliminates the frequency dependence of $\vec{\mathbb{G}}(\omega)$ by fixing $\vec{\mathbb{G}}(\omega) = \vec{\mathbb{G}}(\omega_{sp})$, where ω_{sp} is the quasistatic LSP resonance frequency. This simplification, along with the use of the quasistatic polarizability extended to include the leading order scattering correction to $\alpha(\omega)$, both of which are suitable approximations given the small particle sizes and longitudinal coupling considered in that work, greatly simplifies the identification of eigenfrequencies. However, for the large particle radii and the scattering-mediated diffractive coupling considered in our work, the fully retarded $\alpha(\omega)$ is determined from the $a_1(\omega)$ Mie scattering coefficient, which does not have a simple ω dependence, and the full frequency dependence of $\vec{\mathbb{G}}(\omega)$ must be retained.

We proceed, therefore, by searching numerically for the complex-valued eigenfrequencies ω_r that satisfy the eigenproblem by being roots of the function $f(\omega) = |\det\vec{\mathbf{A}}(\omega)|$. This converts the search for complex eigenfrequencies into a search for minima (i.e., roots) on the nonlinear $|\det\vec{\mathbf{A}}(\omega)|$ surface. Because the nonlinearity of the surface precludes the application of common minimization techniques such as gradient descent algorithms, we perform a grid search over finite domains of real and imaginary frequency space to identify minima of the $|\det\vec{\mathbf{A}}(\omega)|$ surface and the corresponding eigenfrequencies ω_r. Due to the need to evaluate the sphere polarizability inverse, and therefore the Ag dielectric function $\varepsilon(\omega)$ at complex frequencies, an analytic Drude model is used. Drude model parameters ($\varepsilon_\infty = 5$, $\hbar\gamma = 0.0387$ eV, and $\hbar\omega_p = 8.9$ eV) were taken from ref 80. A representative example of such an eigenfrequency search is shown in Figure 7.

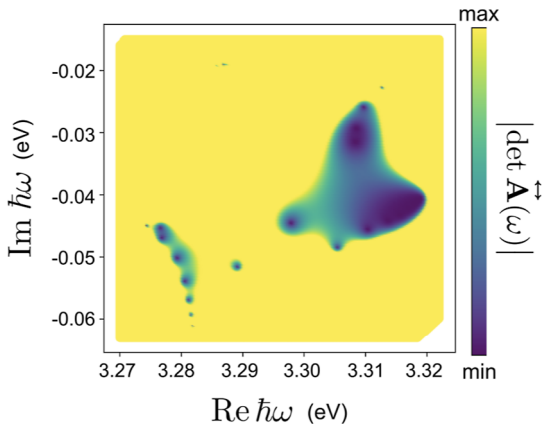

Figure 7. Contour plot of $|\det\vec{\mathbf{A}}(\omega)|$, defined in eq 10, as a function of the complex-valued energy $\hbar\omega$. The darkest points indicate locations of the eigenenergies $\hbar\omega_r$, where $|\det\vec{\mathbf{A}}(\omega_r)| \approx 0$.

Eigenenergies $\hbar\omega_r$ located using this approach for a finite 10 unit cell portion of the $d = 250$ nm, $t = 100$ nm homodimer lattice are shown in Figure 5a superimposed over the absorption dispersion diagram. The red and blue bullets in Figure 5a are the values $Re\ \hbar\omega_r$ determined using $\vec{\mathbb{G}}(\omega_r)$ and $\vec{\mathbb{G}}(\omega_{sp})$, respectively, during the minimization procedure. To find the eigenvector associated with each ω_r, the $\vec{\mathbb{G}}(\omega_r)$ matrix is constructed and diagonalized numerically, yielding a new set of eigenvalues $\{\lambda_n\}$. We select the eigenvector $\mathbf{P}_r(\omega_r)$ corresponding to the numerically determined eigenvalue λ_n closest to $\alpha^{-1}(\omega_r)$. This procedure for calculating eigenvectors is appropriate because $[\alpha^{-1}(\omega)\mathbb{I}, \vec{\mathbb{G}}(\omega)] = 0$, which is the case for all monomer and homodimer lattices considered herein.

The same minimization procedure can be applied in the reciprocal space to identify a set of eigenfrequencies and associated eigenvectors at each value of $k_\parallel$ for the infinite 1D

https://doi.org/10.1021/acsphotonics.2c01155
ACS Photonics 2022, 9, 3656−3667

homodimer array by locating ω_r such that $|\det\vec{\vec{\mathcal{A}}}(k_{||}, \omega_r)| = 0$. The reciprocal space coupling matrix in this case is $\vec{\vec{\mathcal{A}}}(k_{||}, \omega) = \alpha^{-1}(\omega)\vec{\vec{\mathbb{I}}} - \vec{\vec{\mathcal{G}}}(k_{||}, \omega)$, where

$$\vec{\vec{\mathcal{G}}}(k_{||}, \omega) = \begin{bmatrix} \vec{\vec{\mathbf{S}}}(k_{||}, \omega) & \vec{\vec{\mathbf{T}}}_{AB}(k_{||}, \omega) \\ \vec{\vec{\mathbf{T}}}_{BA}(k_{||}, \omega) & \vec{\vec{\mathbf{S}}}(k_{||}, \omega) \end{bmatrix} \tag{11}$$

The white open circles in Figure 5a show $Re\ \hbar\omega_r$ versus $k_{||}$ for the infinite 1D homodimer array calculated using this reciprocal space eigensolver approach and exhibit close agreement with the absorption spectra of the plane wave forced system displayed as the underlying color map. Reciprocal space eigenvectors $\mathbf{P}_r^T(k_{||}, \omega_r) = [\mathbf{p}_A^T(k_{||}, \omega_r)\ \mathbf{p}_B^T(k_{||}, \omega_r)]$ can then be found using the same procedure used to find eigenvectors for the site space problem.

The reciprocal space eigenvectors are used to evaluate the Zak phase $\gamma_\beta = [\phi^\beta_{k_{||}=X} - \phi^\beta_{k_{||}=-X}]/2$, where $\phi^\beta_{k_{||}}$ is the relative phase between the relevant induced dipole moment components on sublattice sites A and B for the right (or left) reciprocal space eigenvectors at Bloch vector $k_{||}$. For example, γ_x for the transversely polarized case is evaluated using

$$\phi^x_{k_{||}} = \mathrm{Arg}\{\mathbf{p}_A(k_{||})\cdot\hat{\mathbf{x}}\} - \mathrm{Arg}\{\mathbf{p}_B(k_{||})\cdot\hat{\mathbf{x}}\} \tag{12}$$

at the $\pm$X points ($k_{||} = \pm\pi/d$).

■ ASSOCIATED CONTENT

Supporting Information

The Supporting Information is available free of charge at https://pubs.acs.org/doi/10.1021/acsphotonics.2c01155.

Size-dependent absorption spectra of individual Ag nanospheres; monomer lattice response under longitudinal and transverse incident polarization; and transverse eigenvectors of the finite homodimer lattice (PDF)

■ AUTHOR INFORMATION

Corresponding Author

David J. Masiello − *Department of Chemistry, University of Washington, Seattle, Washington 98195-1700, United States; Department of Materials Science and Engineering, University of Washington, Seattle, Washington 98195-1700, United States;* orcid.org/0000-0002-1187-0920; Email: masiello@uw.edu

Authors

Marc R. Bourgeois − *Department of Chemistry, University of Washington, Seattle, Washington 98195-1700, United States;* orcid.org/0000-0002-9435-9051

Andrew W. Rossi − *Department of Chemistry, University of Washington, Seattle, Washington 98195-1700, United States;* orcid.org/0000-0001-7588-534X

Siamak Khorasani − *Department of Materials Science and Engineering, University of Washington, Seattle, Washington 98195-1700, United States;* orcid.org/0000-0003-4395-6910

Complete contact information is available at: https://pubs.acs.org/10.1021/acsphotonics.2c01155

Funding

This work was supported by the U.S. National Science Foundation under grant nos. CHE-2118333 and CHE-1954393.

Notes

The authors declare no competing financial interest.

■ ACKNOWLEDGMENTS

This work was supported by the computational, storage, and networking infrastructure provided by the Hyak supercomputer system at the University of Washington. Additionally, we thank Katherine A. Willets and Stephan Link for helpful discussions on experimental measurements of thermal gradients in plasmonic NP systems.

■ REFERENCES

(1) Qiu, J.; Wei, W. D. Surface plasmon-mediated photothermal chemistry. *J. Phys. Chem. C* **2014**, *118*, 20735−20749.

(2) Cao, L.; Barsic, D. N.; Guichard, A. R.; Brongersma, M. L. Plasmon-assisted local temperature control to pattern individual semiconductor nanowires and carbon nanotubes. *Nano Lett.* **2007**, *7*, 3523−3527.

(3) Mateo, D.; Cerrillo, J. L.; Durini, S.; Gascon, J. Fundamentals and applications of photo-thermal catalysis. *Chem. Soc. Rev.* **2021**, *50*, 2173−2210.

(4) Vázquez-Vázquez, C.; Vaz, B.; Giannini, V.; Pérez-Lorenzo, M.; Alvarez-Puebla, R. A.; Correa-Duarte, M. A. Nanoreactors for simultaneous remote thermal activation and optical monitoring of chemical reactions. *J. Am. Chem. Soc.* **2013**, *135*, 13616−13619.

(5) Zhou, N.; Xu, X.; Hammack, A. T.; Stipe, B. C.; Gao, K.; Scholz, W.; Gage, E. C. Plasmonic near-field transducer for heat-assisted magnetic recording. *Nanophotonics* **2014**, *3*, 141−155.

(6) Cheng, F.; Wang, C.; Su, Z.; Wang, X.; Cai, Z.; Sun, N. X.; Liu, Y. All-optical manipulation of magnetization in ferromagnetic thin films enhanced by plasmonic resonances. *Nano Lett.* **2020**, *20*, 6437−6443.

(7) Dolinšek, J.; Feuerbacher, M.; Jagodič, M.; Jagličić, Z.; Heggen, M.; Urban, K. A thermal memory cell. *J. Appl. Phys.* **2009**, *106*, 043917.

(8) Hu, R.; Huang, S.; Wang, M.; Zhou, L.; Peng, X.; Luo, X. Binary thermal encoding by energy shielding and harvesting units. *Phys. Rev. Appl.* **2018**, *10*, 054032.

(9) Manik, R.; Behera, A. Thermal encoding using shape memory alloy. *Mater. Today Proc.* **2020**, *33*, 5709−5713.

(10) Wu, Y.; Qu, Z.; Osman, A.; Cao, W.; Khokhar, A. Z.; Soler Penades, J.; Muskens, O. L.; Mashanovich, G. Z.; Nedeljkovic, M. Mid-infrared nanometallic antenna assisted silicon waveguide based bolometers. *ACS Photonics* **2019**, *6*, 3253−3260.

(11) Kong, X.-T.; Khosravi Khorashad, L.; Wang, Z.; Govorov, A. O. Photothermal circular dichroism induced by plasmon resonances in chiral metamaterial absorbers and bolometers. *Nano Lett.* **2018**, *18*, 2001−2008.

(12) Huang, X.; Jain, P. K.; El-Sayed, I. H.; El-Sayed, M. A. Plasmonic Photothermal therapy (PPTT) using gold nanoparticles. *Laser Med. Sci.* **2008**, *23*, 217−228.

(13) Ali, M. R.; Wu, Y.; El-Sayed, M. A. Gold-nanoparticle-assisted plasmonic photothermal therapy advances toward clinical application. *J. Phys. Chem. C* **2019**, *123*, 15375−15393.

(14) Qiu, G.; Gai, Z.; Tao, Y.; Schmitt, J.; Kullak-Ublick, G. A.; Wang, J. Dual-functional plasmonic photothermal biosensors for highly accurate severe acute respiratory syndrome coronavirus 2 detection. *ACS Nano* **2020**, *14*, 5268−5277.

(15) Baffou, G.; Quidant, R. Thermo-plasmonics: using metallic nanostructures as nano-sources of heat. *Laser Photon. Rev.* **2013**, *7*, 171−187.

(16) Baffou, G.; Cichos, F.; Quidant, R. Applications and challenges of thermoplasmonics. *Nat. Mater.* **2020**, *19*, 946−958.

(17) Hartland, G. V. Optical studies of dynamics in noble metal nanostructures. *Chem. Rev.* **2011**, *111*, 3858−3887.
(18) Govorov, A. O.; Zhang, W.; Skeini, T.; Richardson, H.; Lee, J.; Kotov, N. A. Gold nanoparticle ensembles as heaters and actuators: melting and collective plasmon resonances. *Nanoscale Res. Lett.* **2006**, *1*, 84−90.
(19) Jauffred, L.; Samadi, A.; Klingberg, H.; Bendix, P. M.; Oddershede, L. B. Plasmonic heating of nanostructures. *Chem. Rev.* **2019**, *119*, 8087−8130.
(20) Baffou, G.; Quidant, R.; García de Abajo, F. J. Nanoscale control of optical heating in complex plasmonic systems. *ACS Nano* **2010**, *4*, 709−716.
(21) Coppens, Z. J.; Li, W.; Walker, D. G.; Valentine, J. G. Probing and controlling photothermal heat generation in plasmonic nanostructures. *Nano Lett.* **2013**, *13*, 1023−1028.
(22) Khosravi Khorashad, L.; Besteiro, L. V.; Wang, Z.; Valentine, J.; Govorov, A. O. Localization of excess temperature using plasmonic hot spots in metal nanostructures: combining nano-optical antennas with the Fano effect. *J. Phys. Chem. C* **2016**, *120*, 13215−13226.
(23) Baldwin, C. L.; Bigelow, N. W.; Masiello, D. J. Thermal signatures of plasmonic Fano interferences: toward the achievement of nanolocalized temperature manipulation. *J. Phys. Chem. Lett.* **2014**, *5*, 1347−1354.
(24) Bhattacharjee, U.; West, C. A.; Hosseini Jebeli, S. A.; Goldwyn, H. J.; Kong, X.-T.; Hu, Z.; Beutler, E. K.; Chang, W.-S.; Willets, K. A.; Link, S.; Masiello, D. J. Active far-field control of the thermal near-field via plasmon hybridization. *ACS Nano* **2019**, *13*, 9655−9663.
(25) Hosseini Jebeli, S. A.; West, C. A.; Lee, S. A.; Goldwyn, H. J.; Bilchak, C. R.; Fakhraai, Z.; Willets, K. A.; Link, S.; Masiello, D. J. Wavelength-dependent photothermal imaging probes nanoscale temperature differences among subdiffraction coupled plasmonic nanorods. *Nano Lett.* **2021**, *21*, 5386−5393.
(26) Boyer, D.; Tamarat, P.; Maali, A.; Lounis, B.; Orrit, M. Photothermal Imaging of Nanometer-Sized Metal Particles Among Scatterers. *Science* **2002**, *297*, 1160−1163.
(27) Berciaud, S.; Cognet, L.; Blab, G. A.; Lounis, B. Photothermal Heterodyne Imaging of Individual Nonfluorescent Nanoclusters and Nanocrystals. *Phys. Rev. Lett.* **2004**, *93*, 257402.
(28) Baffou, G.; Berto, P.; Bermúdez Ureña, E.; Quidant, R.; Monneret, S.; Polleux, J.; Rigneault, H. Photoinduced heating of nanoparticle arrays. *ACS Nano* **2013**, *7*, 6478−6488.
(29) Guo, R.; Hakala, T. K.; Törmä, P. Geometry dependence of surface lattice resonances in plasmonic nanoparticle arrays. *Phys. Rev. B* **2017**, *95*, 155423.
(30) Zou, S.; Janel, N.; Schatz, G. C. Silver nanoparticle array structures that produce remarkably narrow plasmon lineshapes. *J. Chem. Phys.* **2004**, *120*, 10871−10875.
(31) Kravets, V. G.; Kabashin, A. V.; Barnes, W. L.; Grigorenko, A. N. Plasmonic surface lattice resonances: a review of properties and applications. *Chem. Rev.* **2018**, *118*, 5912−5951.
(32) Cherqui, C.; Bourgeois, M. R.; Wang, D.; Schatz, G. C. Plasmonic surface lattice resonances: theory and computation. *Acc. Chem. Res.* **2019**, *52*, 2548−2558.
(33) Humphrey, A.; Barnes, W. Plasmonic surface lattice resonances in arrays of metallic nanoparticle dimers. *J. Opt.* **2016**, *18*, 035005.
(34) Humphrey, A. D.; Meinzer, N.; Starkey, T. A.; Barnes, W. L. Surface lattice resonances in plasmonic arrays of asymmetric disc dimers. *ACS Photonics* **2016**, *3*, 634−639.
(35) Baur, S.; Sanders, S.; Manjavacas, A. Hybridization of lattice resonances. *ACS Nano* **2018**, *12*, 1618−1629.
(36) GuO, R.; Nečada, M.; Hakala, T. K.; Väkeväinen, A. I.; Törmä, P. Lasing at K points of a honeycomb plasmonic lattice. *Phys. Rev. Lett.* **2019**, *122*, 013901.
(37) Li, R.; Bourgeois, M. R.; Cherqui, C.; Guan, J.; Wang, D.; Hu, J.; Schaller, R. D.; Schatz, G. C.; Odom, T. W. Hierarchical hybridization in plasmonic honeycomb lattices. *Nano Lett.* **2019**, *19*, 6435−6441.
(38) Lu, L.; Joannopoulos, J. D.; Soljačić, M. Topological photonics. *Nat. Photonics* **2014**, *8*, 821−829.
(39) Rider, M. S.; Buendía, Á.; Abujetas, D. R.; Huidobro, P. A.; Sánchez-Gil, J. A.; Giannini, V. Advances and prospects in topological nanoparticle photonics. *ACS Photonics* **2022**, *9*, 1483−1499.
(40) Novotny, L.; Hecht, B.*Principles of Nano-Optics*, 2nd ed.; Cambridge University Press, 2012.
(41) Purcell, E. M.; Pennypacker, C. R. Scattering and absorption of light by nonspherical dielectric grains. *Astrophys. J.* **1973**, *186*, 705−714.
(42) Draine, B. T.; Flatau, P. J. Discrete-dipole approximation for scattering calculations. *J. Opt. Soc. Am. A* **1994**, *11*, 1491−1499.
(43) Kelly, K. L.; Coronado, E.; Zhao, L. L.; Schatz, G. C. The optical properties of metal nanoparticles: the influence of size, shape, and dielectric environment. *J. Phys. Chem. B* **2003**, *107*, 668−677.
(44) Metwally, K.; Mensah, S.; Baffou, G. Isosbestic thermoplasmonic nanostructures. *ACS Photonics* **2017**, *4*, 1544−1551.
(45) Citrin, D. Plasmon-polariton transport in metal-nanoparticle chains embedded in a gain medium. *Opt. Lett.* **2006**, *31*, 98−100.
(46) Bourgeois, M. R.; Rossi, A. W.; Chalifour, M.; Cherqui, C.; Masiello, D. J. Lattice kerker effect with plasmonic oligomers. *J. Phys. Chem. C* **2021**, *125*, 18817−18826.
(47) Lee, Y.-A. L.; Mousavikhamene, Z.; Amrithanath, A. K.; Neidhart, S. M.; Krishnaswamy, S.; Schatz, G. C.; Odom, T. W. Programmable Self-Regulation with Wrinkled Hydrogels and Plasmonic Nanoparticle Lattices. *Small* **2022**, *18*, 2103865.
(48) Markel, V. A. Coupled-dipole approach to scattering of light from a one-dimensional periodic dipole structure. *J. Mod. Opt.* **1993**, *40*, 2281−2291.
(49) Baffou, G.; Quidant, R.; Girard, C. Thermoplasmonics modeling: A Green's function approach. *Phys. Rev. B: Condens. Matter Mater. Phys.* **2010**, *82*, 165424.
(50) Pocock, S. R.; Xiao, X.; Huidobro, P. A.; Giannini, V. Topological plasmonic chain with retardation and radiative effects. *ACS Photonics* **2018**, *5*, 2271−2279.
(51) Han, D.; Lai, Y.; Zi, J.; Zhang, Z.-Q.; Chan, C. T. Dirac spectra and edge states in honeycomb plasmonic lattices. *Phys. Rev. Lett.* **2009**, *102*, 123904.
(52) Poddubny, A.; Miroshnichenko, A.; Slobozhanyuk, A.; Kivshar, Y. Topological Majorana states in zigzag chains of plasmonic nanoparticles. *ACS Photonics* **2014**, *1*, 101−105.
(53) Sinev, I. S.; Mukhin, I. S.; Slobozhanyuk, A. P.; Poddubny, A. N.; Miroshnichenko, A. E.; Samusev, A. K.; Kivshar, Y. S. Mapping plasmonic topological states at the nanoscale. *Nanoscale* **2015**, *7*, 11904−11908.
(54) Wang, L.; Zhang, R.-Y.; Xiao, M.; Han, D.; Chan, C. T.; Wen, W. The existence of topological edge states in honeycomb plasmonic lattices. *New J. Phys.* **2016**, *18*, 103029.
(55) Jin, D.; Christensen, T.; Soljačić, M.; Fang, N. X.; Lu, L.; Zhang, X. Infrared topological plasmons in graphene. *Phys. Rev. Lett.* **2017**, *118*, 245301.
(56) Bleckmann, F.; Cherpakova, Z.; Linden, S.; Alberti, A. Spectral imaging of topological edge states in plasmonic waveguide arrays. *Phys. Rev. B* **2017**, *96*, 045417.
(57) Zhang, W.; Chen, X.; Ye, F. Plasmonic topological insulators for topological nanophotonics. *Opt. Lett.* **2017**, *42*, 4063−4066.
(58) Qiu, P.; Liang, R.; Qiu, W.; Chen, H.; Ren, J.; Lin, Z.; Wang, J.-X.; Kan, Q.; Pan, J.-Q. Topologically protected edge states in graphene plasmonic crystals. *Opt. Express* **2017**, *25*, 22587−22594.
(59) Su, W.; Schrieffer, J.; Heeger, A. J. Solitons in polyacetylene. *Phys. Rev. Lett.* **1979**, *42*, 1698.
(60) Downing, C. A.; Weick, G. Topological plasmons in dimerized chains of nanoparticles: robustness against long-range quasistatic interactions and retardation effects. *Eur. Phys. J. B* **2018**, *91*, 253.
(61) Martinez Alvarez, V.; Barrios Vargas, J.; Berdakin, M.; Foa Torres, L. Topological states of non-Hermitian systems. *Eur. Phys. J. Spec. Top.* **2018**, *227*, 1295−1308.
(62) Fernique, F.; Weick, G. Plasmons in two-dimensional lattices of near-field coupled nanoparticles. *Phys. Rev. B* **2020**, *102*, 045420.
(63) Li, M.; Zhirihin, D.; Gorlach, M.; Ni, X.; Filonov, D.; Slobozhanyuk, A.; Alù, A.; Khanikaev, A. B. Higher-order topological

states in photonic kagome crystals with long-range interactions. *Nat. Photonics* **2020**, *14*, 89−94.
(64) Pocock, S. R.; Huidobro, P. A.; Giannini, V. Bulk-edge correspondence and long-range hopping in the topological plasmonic chain. *Nanophotonics* **2019**, *8*, 1337−1347.
(65) Zak, J. Berry's phase for energy bands in solids. *Phys. Rev. Lett.* **1989**, *62*, 2747.
(66) Bohren, C. F.; Huffman, D. R.*Absorption and Scattering of Light by Small Particles*; John Wiley & Sons, 2008.
(67) Lieu, S. Topological phases in the non-Hermitian Su-Schrieffer-Heeger model. *Phys. Rev. B* **2018**, *97*, 045106.
(68) Yao, S.; Wang, Z. Edge states and topological invariants of non-Hermitian systems. *Phys. Rev. Lett.* **2018**, *121*, 086803.
(69) Wang, B.; Zhao, C. Topological phonon polaritons in one-dimensional non-Hermitian silicon carbide nanoparticle chains. *Phys. Rev. B* **2018**, *98*, 165435.
(70) Wang, B. X.; Zhao, C. Terahertz topological plasmon polaritons for robust temperature sensing. *Phys. Rev. Mater.* **2020**, *4*, 075201.
(71) Wang, B.; Zhao, C. Topological photonic states in one-dimensional dimerized ultracold atomic chains. *Phys. Rev. A* **2018**, *98*, 023808.
(72) Lee, C. H.; Thomale, R. Anatomy of skin modes and topology in non-Hermitian systems. *Phys. Rev. B* **2019**, *99*, 201103.
(73) Ott, A.; Biehs, S.-A. Radiative heat flux through a topological Su-Schrieffer-Heeger chain of plasmonic nanoparticles. *Phys. Rev. B* **2020**, *102*, 115417.
(74) Yang, A.; Hryn, A. J.; Bourgeois, M. R.; Lee, W.-K.; Hu, J.; Schatz, G. C.; Odom, T. W. Programmable and reversible plasmon mode engineering. *Proc. Natl. Acad. Sci. U.S.A.* **2016**, *113*, 14201−14206.
(75) Wang, D.; Bourgeois, M. R.; Lee, W.-K.; Li, R.; Trivedi, D.; Knudson, M. P.; Wang, W.; Schatz, G. C.; Odom, T. W. Stretchable nanolasing from hybrid quadrupole plasmons. *Nano Lett.* **2018**, *18*, 4549−4555.
(76) Evlyukhin, A. B.; Reinhardt, C.; Zywietz, U.; Chichkov, B. N. Collective resonances in metal nanoparticle arrays with dipole-quadrupole interactions. *Phys. Rev. B: Condens. Matter Mater. Phys.* **2012**, *85*, 245411.
(77) Cherqui, C.; Bigelow, N. W.; Vaschillo, A.; Goldwyn, H.; Masiello, D. J. Combined tight-binding and numerical electrodynamics understanding of the STEM/EELS magneto-optical responses of aromatic plasmon-supporting metal oligomers. *ACS Photonics* **2014**, *1*, 1013−1024.
(78) Gabrys, P. A.; Zornberg, L. Z.; Macfarlane, R. J. Programmable atom equivalents: atomic crystallization as a framework for synthesizing nanoparticle superlattices. *Small* **2019**, *15*, 1805424.
(79) Greybush, N. J.; Liberal, I.; Malassis, L.; Kikkawa, J. M.; Engheta, N.; Murray, C. B.; Kagan, C. R. Plasmon resonances in self-assembled two-dimensional Au nanocrystal metamolecules. *ACS Nano* **2017**, *11*, 2917−2927.
(80) Yang, H. U.; D'Archangel, J.; Sundheimer, M. L.; Tucker, E.; Boreman, G. D.; Raschke, M. B. Optical dielectric function of silver. *Phys. Rev. B: Condens. Matter Mater. Phys.* **2015**, *91*, 235137.

https://doi.org/10.1021/acsphotonics.2c01155
ACS Photonics 2022, 9, 3656−3667